Supplement of Solid Earth, 17, 453–464, 2026
https://doi.org/10.5194/se-17-453-2026-supplement

Supplement of

Offshore crustal thickness variation along the Palu–Koro strike–slip fault in the Sulawesi region from OBS receiver function analysis

Tingwei Yang et al.

Correspondence to: ChuanChuan Lü (chuanchuanlu@esc.cam.ac.uk)

Contents of this file

Figure S1 to S12.

Supplementary Figures

Here we provide supplementary figures illustrating key data processing and analysis steps. Figure S1 showing after the clock drift correction, we validate our data's timestamp by cross-correlating the ambient noise between two OBSs (M01G & M02F). Figure S2 presents the azimuth correction conducted based on minimization of tangential component of P-wave energy. Figure S3 compares the raw and pre-processed data. Figure. S4 displays the temporal variation of the ambient noise power spectral density (PSD) at OBS M01G and land station BKB. Figure. S5 showing the probability power spectral density distribution (PPSD) of ambient noise PSD at OBS M01G and land station BKB. Figure. S6-S11 showing the receiver function waveform inversion result for each OBS. Figure. S12 showing the H-κ stacking result of the OBSs.

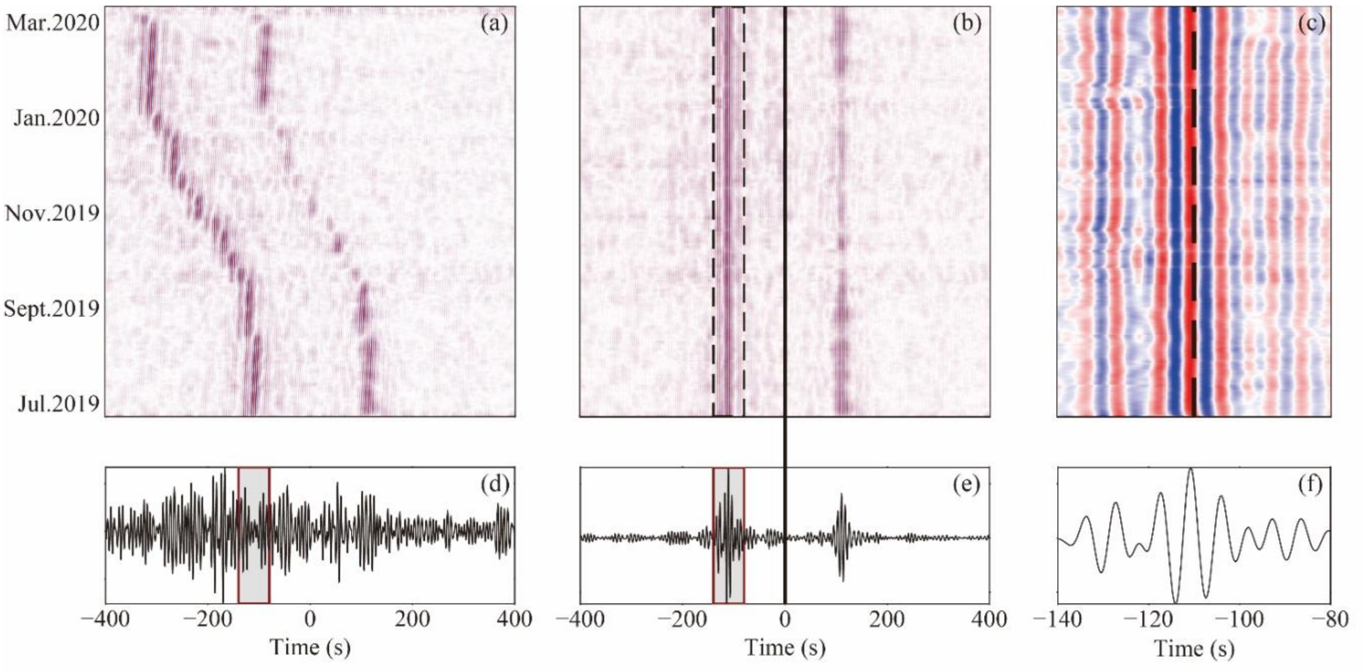

Figure S1: The (a) before and (b) after time-drift corrected CCFs pair (M01G & M02F); (c)Noncausal signals of time corrected ambient noise CCFs; (d) before and (e) after time-drift corrected ambient noise cross correlation function after stacking; (f) noncausal signal of time-drift corrected ambient noise CCFs after stacking.

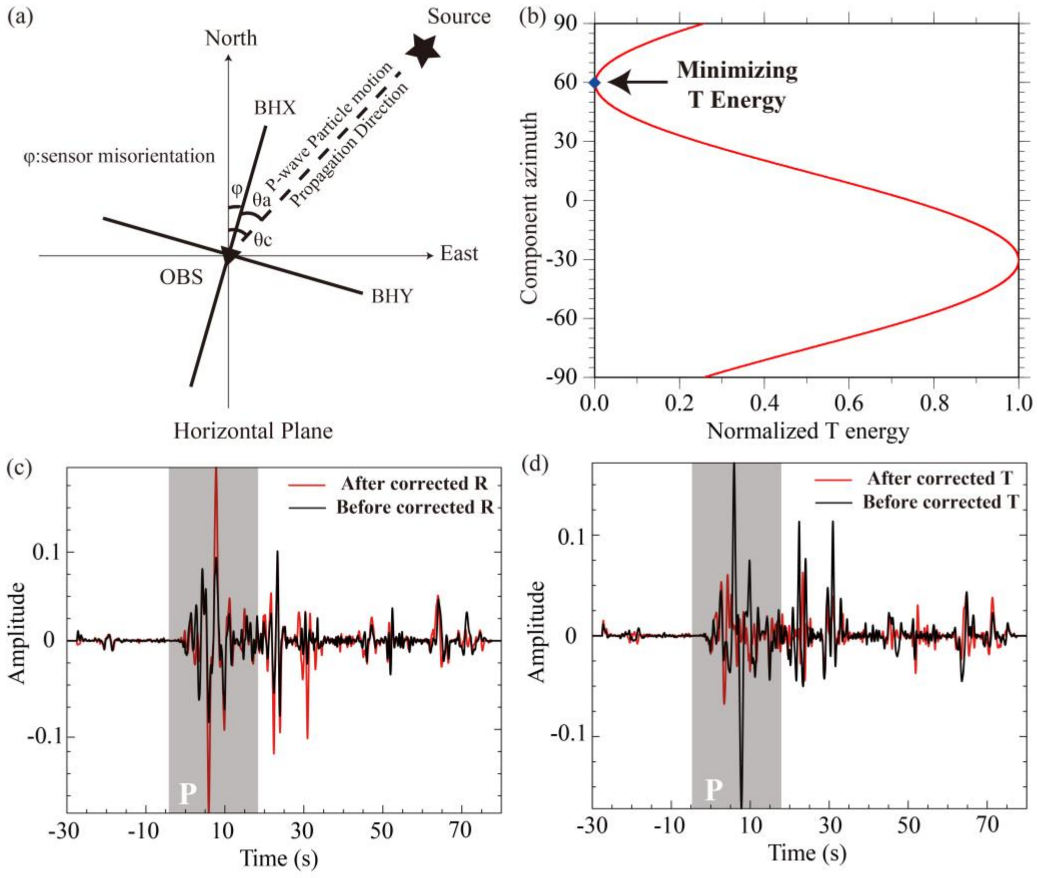

Figure S2: Horizontal azimuth correction for minimizing P-wave T component energy of OBS M01G. (a) Schematic diagram of horizontal azimuth deviation, where φ is the clockwise azimuth deviation between the geographical North Pole and the BHX sensor; θ_c

is the backazimuth calculated by OBS and source position geometry; θ_a is the backazimuth measured by the motion of P-wave particle); (b) Schematic search diagram of P-wave T component energy; Comparison of P-wave waveform of (c) R and (d) T components before and after azimuth correction.

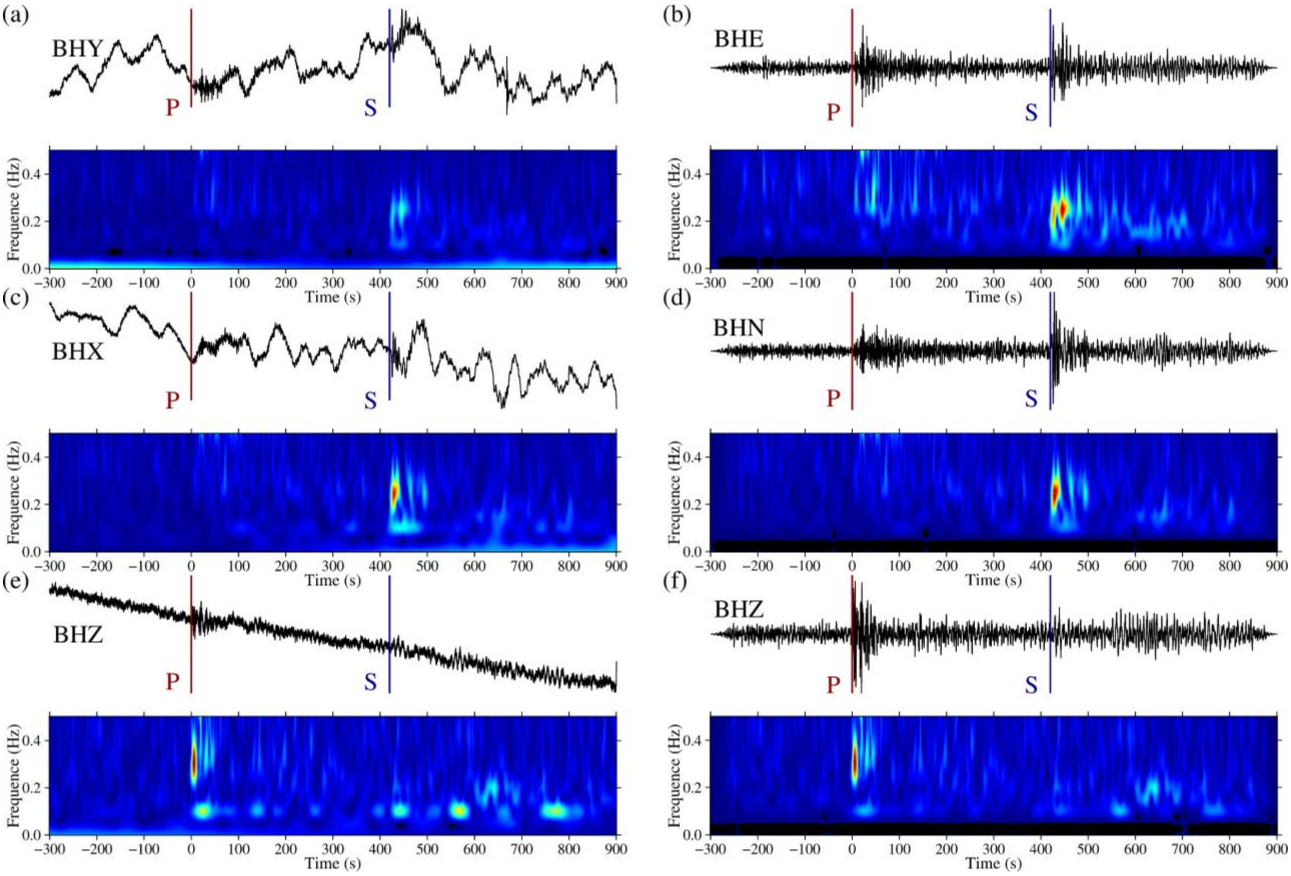

Figure S3: Three components waveform of OBS and its results of wavelet transform. (c) and (e)are respectively indicate components BHY, BHX and BHZ of OBS raw data; (b), (d) and (f) are respectively indicate components BHE, BHN and BHZ of Processed OBS data.

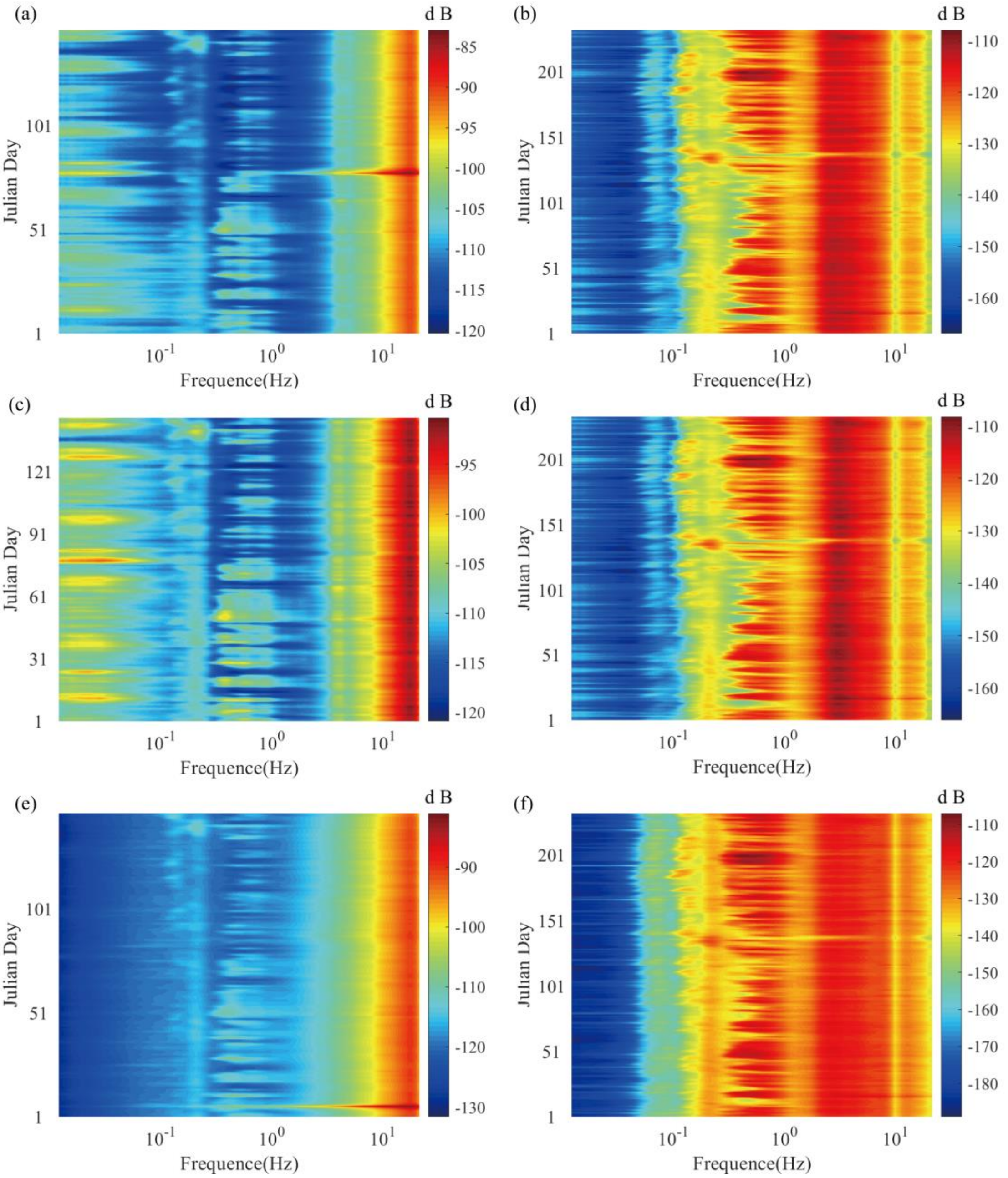

Figure S4: Temporal variation of ambient noise power spectral density of the three components OBS M01G and land station BKB. (a), (c) and (e) are respectively indicate components BHE, BHN and BHZ; (b), (d) and (f) are respectively indicate components BHE, BHN and BHZ of land station BKB.

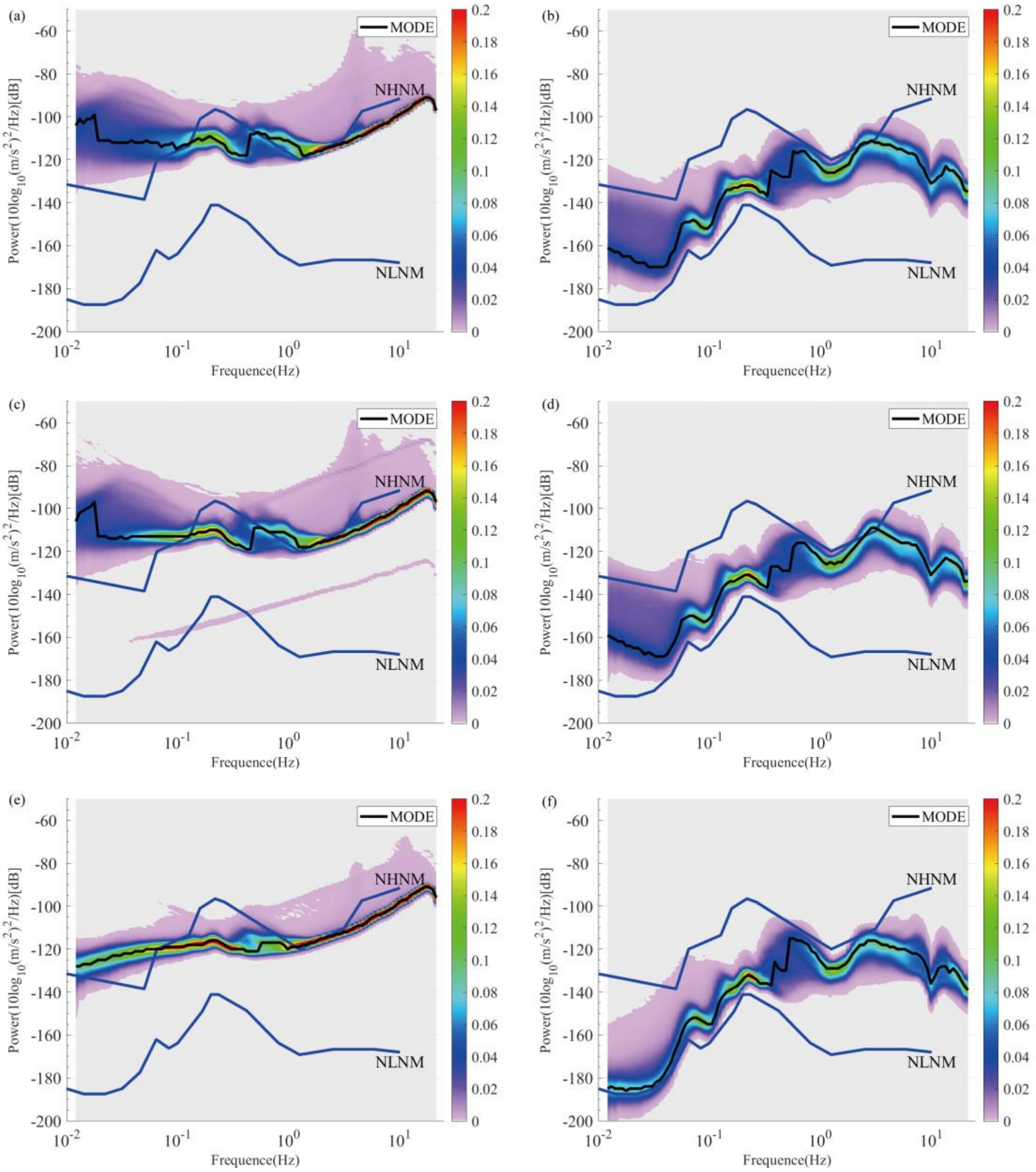

Figure S5: The probability power spectral density distribution (PPSD) of ambient noise PSD at OBS M01G and land stations BKB. (a), (c) and (e) are respectively indicate components BHE, BHN and BHZ of OBS M01G; (b), (d) and (f) are respectively indicate components BHE, BHN and BHZ of land station BKB (black line MODE highlights the typical noise level, blue lines NHNM and NLNM represent the global high and low noise models, respectively).

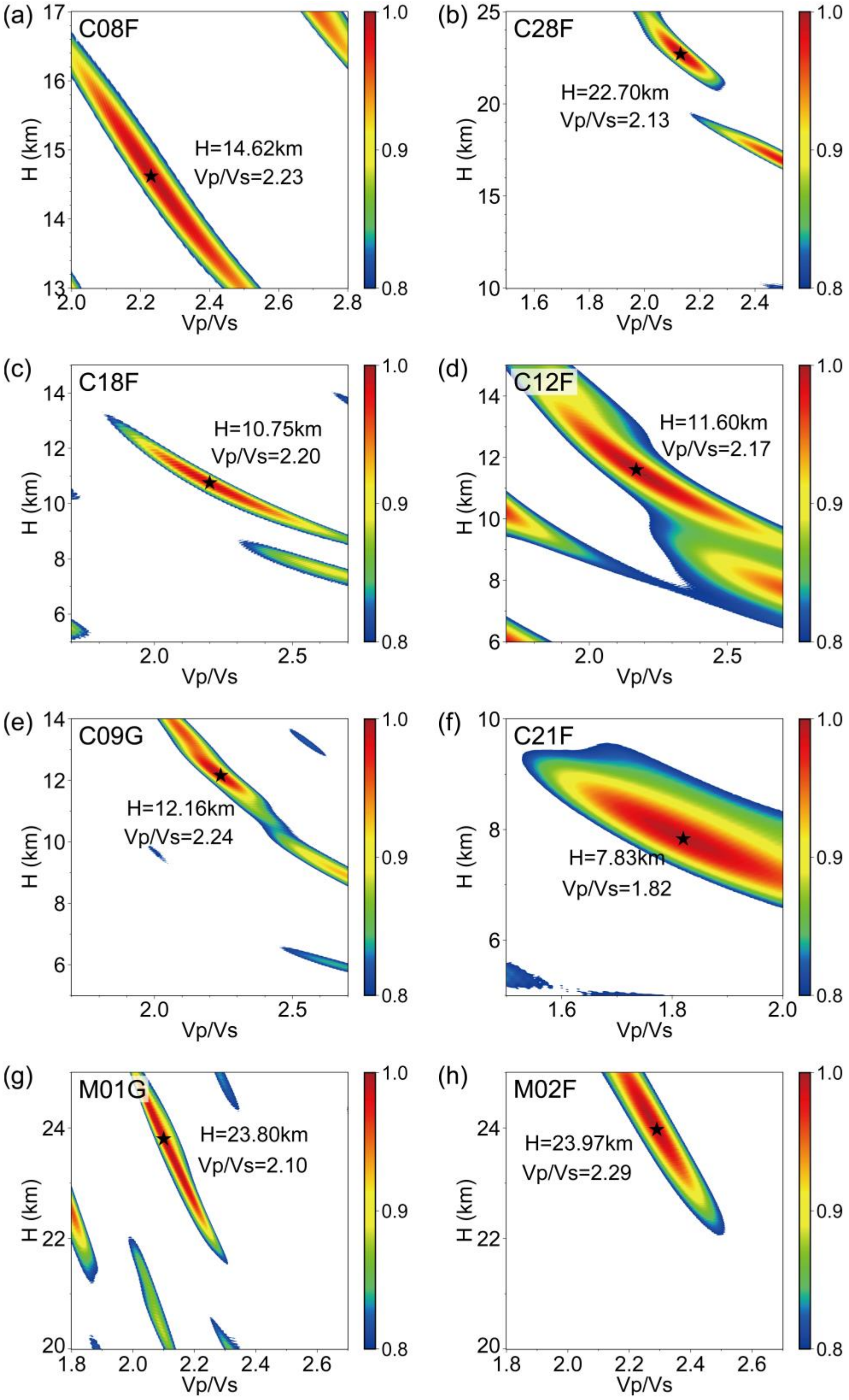

Figure S6: H-κ stacking result of OBS (C08F, C28F, C09G, C12F, C21F, M01G, M02F). The position of the five-pointed star indicates the best solution for H–κ Stacking.

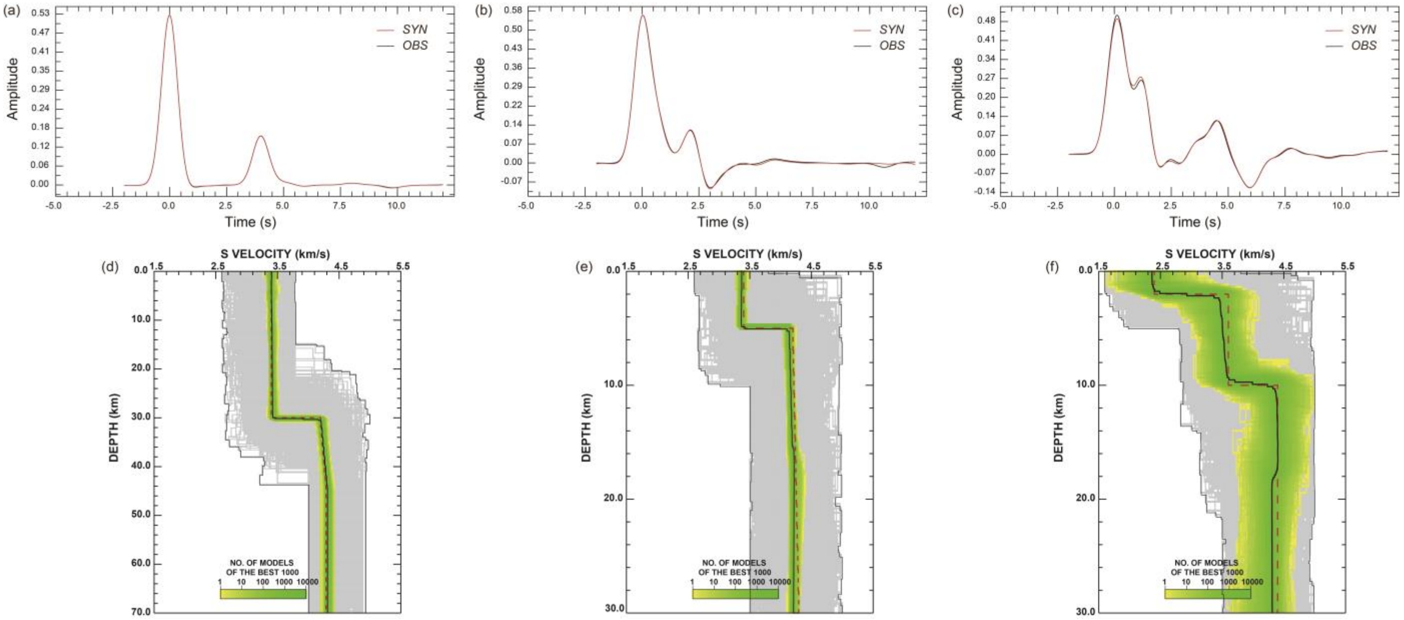

Figure S7: (a–c) Receiver function waveform comparisons for the crustal model, oceanic crustal model, and oceanic crustal model with sediment cover. The black line represents the observed receiver function, while the red line shows the predicted receiver function from the optimal model. (d–f) S-wave velocity structures derived from the Neighborhood Algorithm (NA) inversion. The thin black lines outline the search space, the bold black curve represents the average velocity structure of the 1,000 best-fitting models).

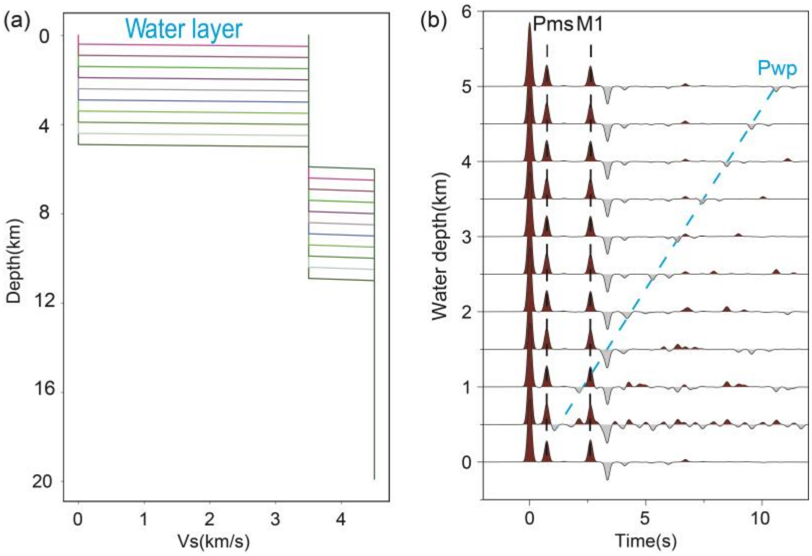

Figure S8: (a) Models with varying water depths. (b) Synthetic receiver functions of the water-layer models. The blue dotted line marks the Pwp phase, representing P-wave transmitted into the seawater.

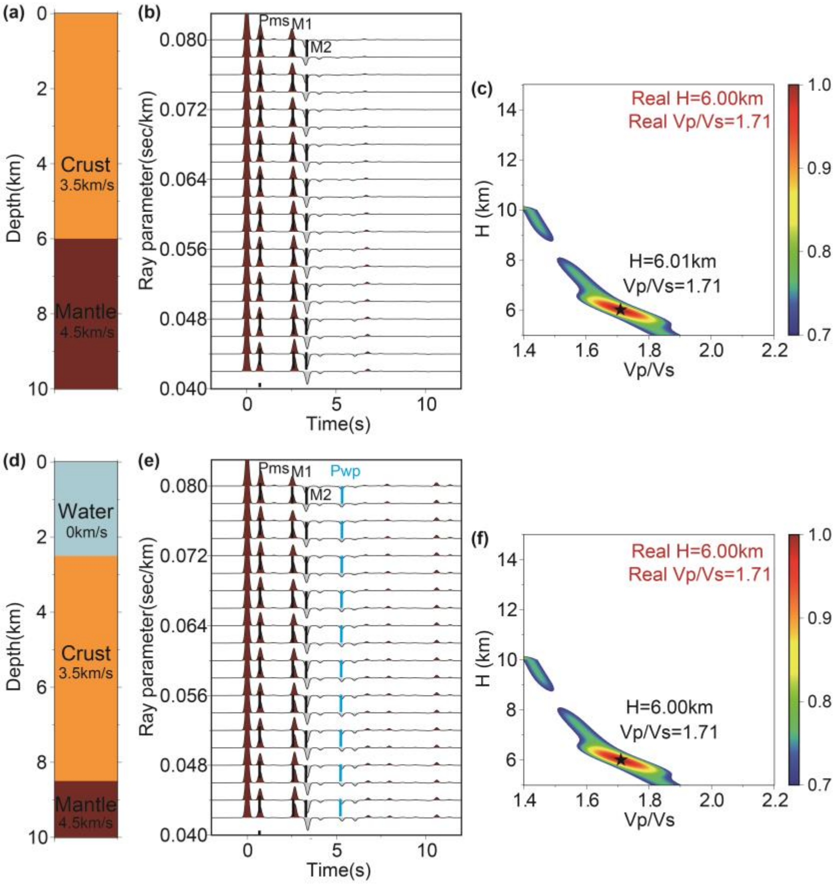

Figure S9: (a) Crustal model and (d) Oceanic crust model. (b) and (e) Synthetic receiver functions. (c) and (f) H-κ stacking result.

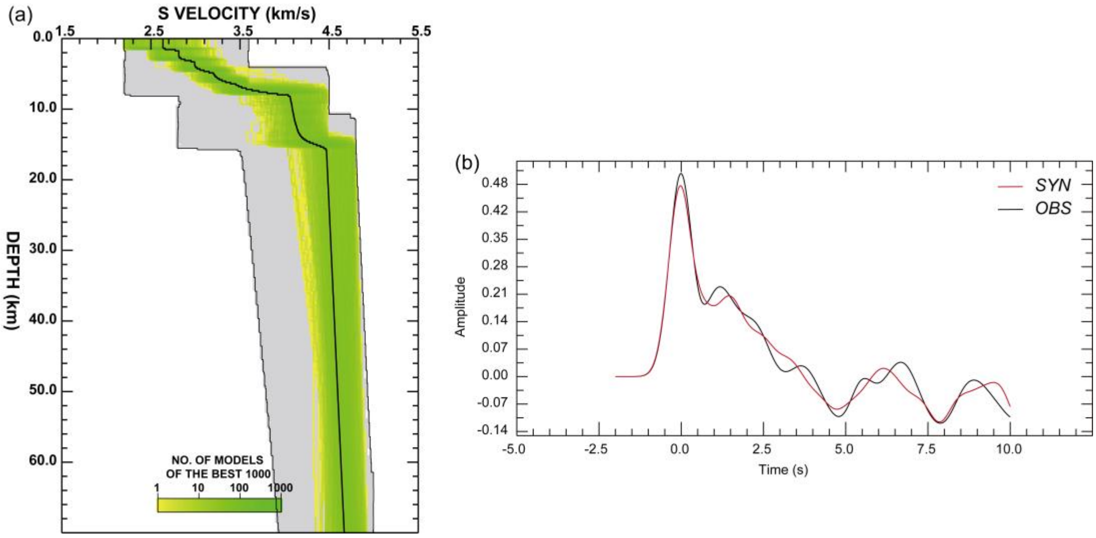

Figure S10: Receiver function waveform inversion results at OBS site C08F. (a) S-wave velocity structure obtained from the NA inversion (The thin black lines outline the search area and the black curve is the average velocity structure of the 1000 best models). (b) Receiver function waveform comparison, where the black line denotes the observed receiver function and the red line shows the receiver function predicted by the optimal model).

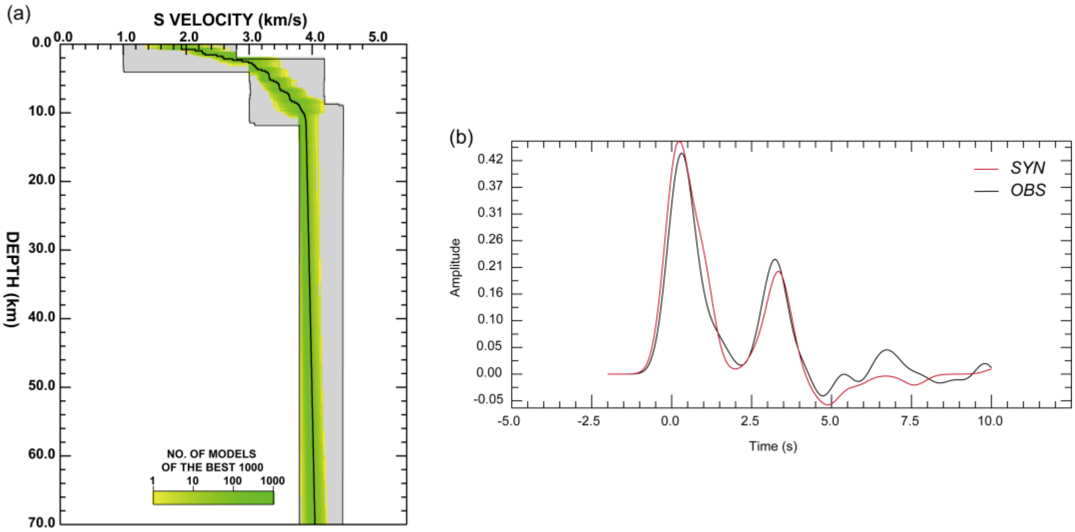

Figure S11: Receiver function waveform inversion results at OBS site C09G. (a) S-wave velocity structure obtained from the NA inversion (The thin black lines outline the search area and the black curve is the average velocity structure of the 1000 best models). (b) Receiver function waveform comparison, where the black line denotes the observed receiver function and the red line shows the receiver function predicted by the optimal model).

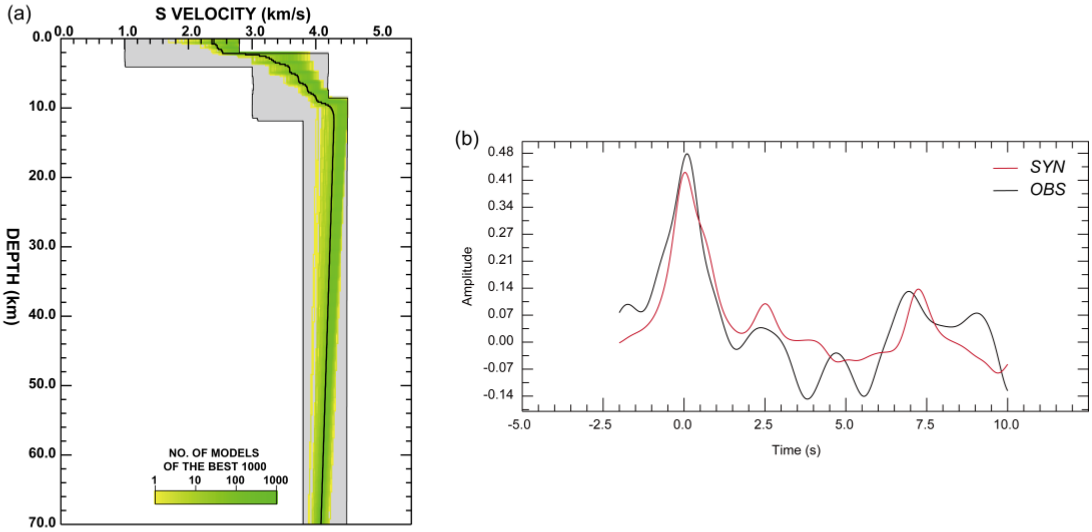

Figure S12: Receiver function waveform inversion results at OBS site C12F. (a) S-wave velocity structure obtained from the NA inversion (The thin black lines outline the search area and the black curve is the average velocity structure of the 1000 best models). (b) Receiver function waveform comparison, where the black line denotes the observed receiver function and the red line shows the receiver function predicted by the optimal model).

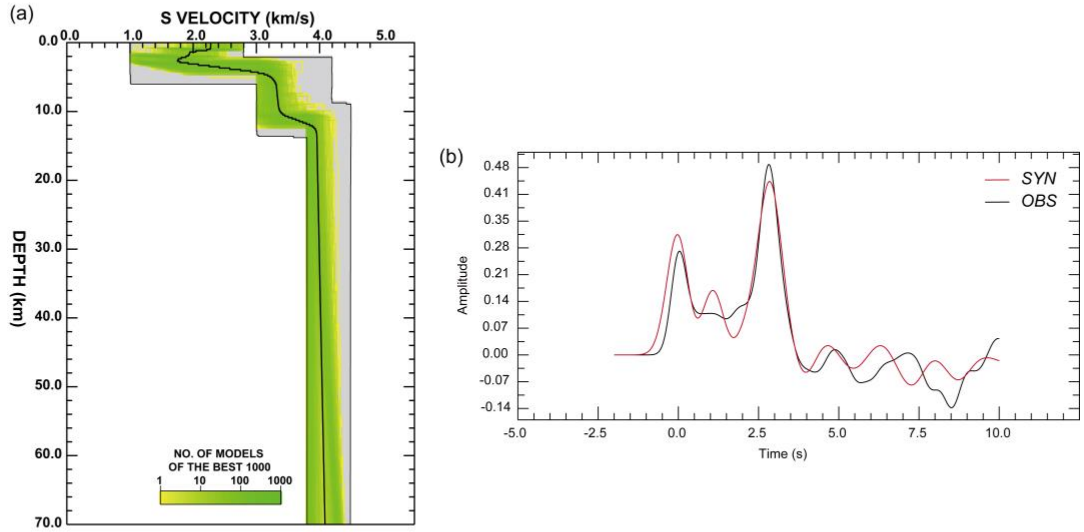

(a)

Figure S13: Receiver function waveform inversion result at OBS site C18F. (a) S-wave velocity structure obtained from the NA inversion (The thin black lines outline the search area and the black curve is the average velocity structure of the 1000 best models). (b) Receiver function waveform comparison where the black line is the observed receiver function and the red line shows the receiver function predicted by the optimal model).

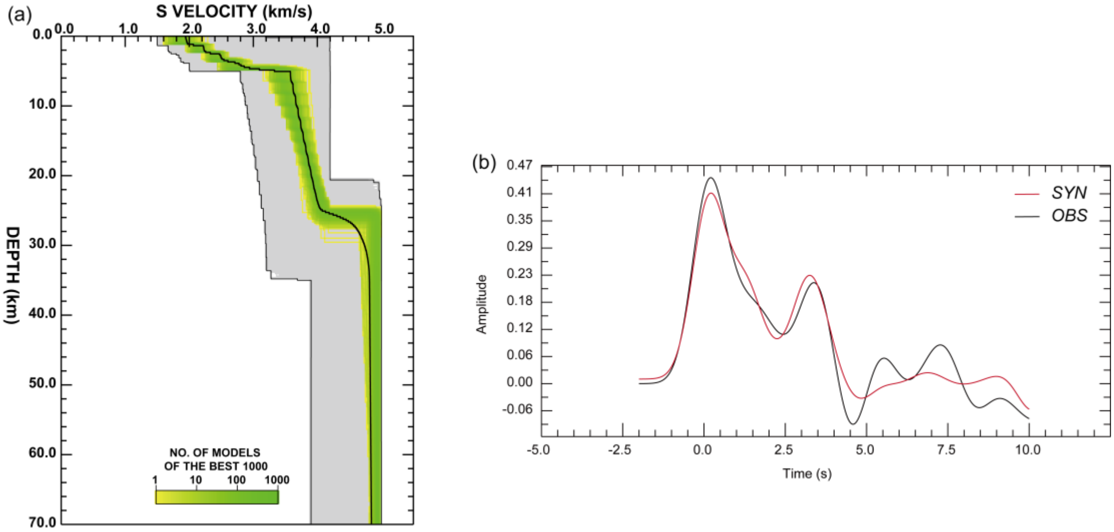

Figure S14: Receiver function waveform inversion results at OBS site M01G. (a) S-wave velocity structure obtained by the NA inversion (The thin black lines outline the search area and the black curve is the average velocity structure of the 1000 best models). (b) Receiver function waveform comparison, where the black line denotes the observed receiver function and the red line shows the receiver function predicted by the optimal model.

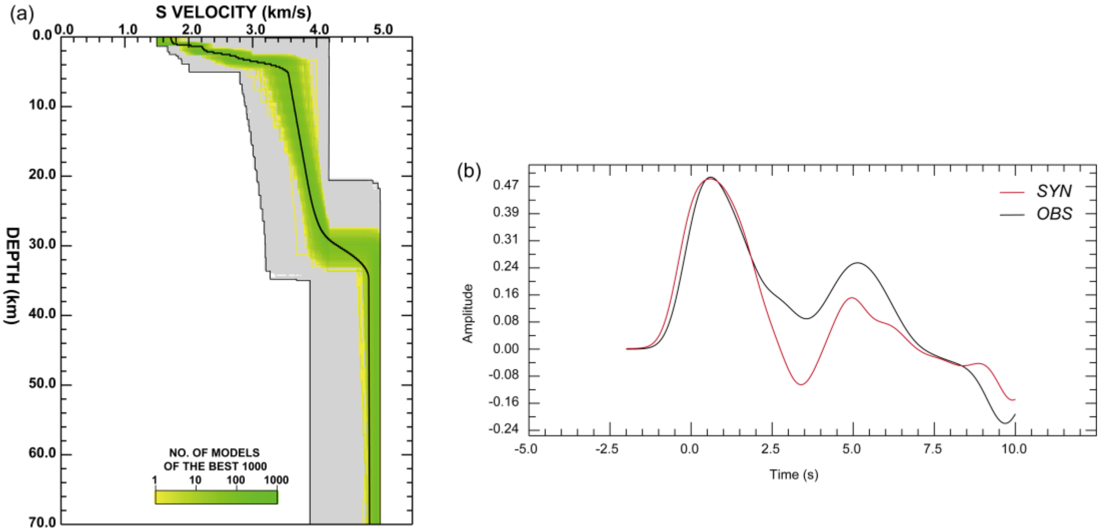

Figure S15: Receiver function waveform inversion results at OBS site M02F. (a) S-wave velocity structure obtained from the NA inversion (The thin black lines outline the search area and the black curve is the average velocity structure of the 1000 best models). (b) Receiver function waveform comparison, where the black line denotes the observed receiver function and the red line shows the receiver function predicted by the optimal model.

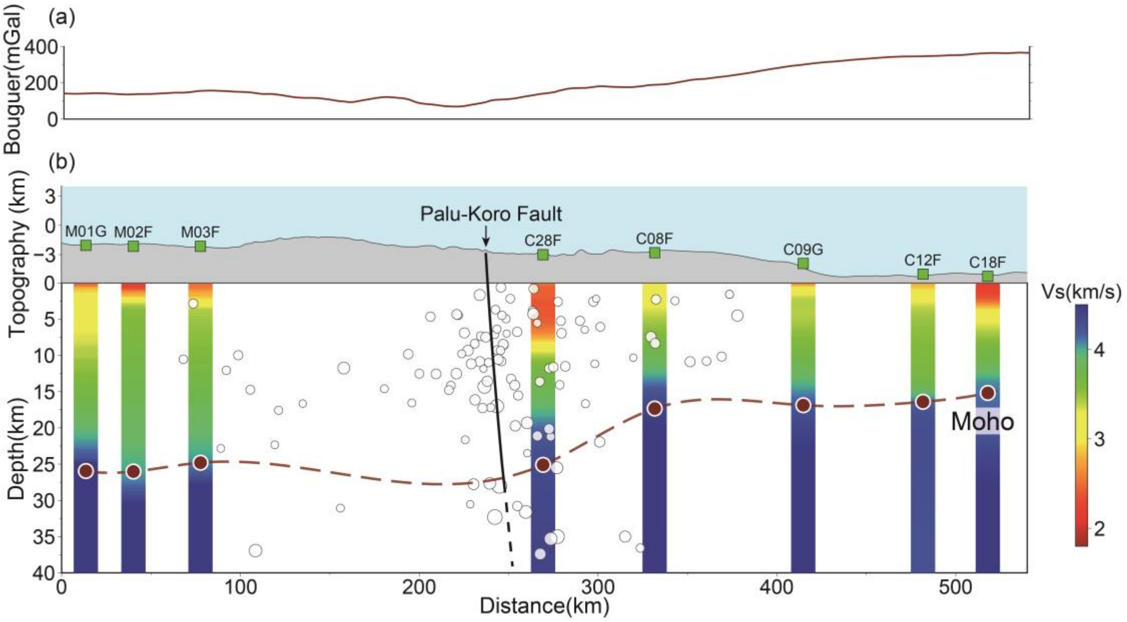

Figure S16: RF waveform inversion results projected on one profie (a) Bouguer anomaly profile across the Palu–Koro fault zone (data from WGM2012, Bonvalot et al., 2009). (b) S-wave velocity (Vs) structure along the same profile.

Text S1: Time correction

Clock drift refers to the small but cumulative timekeeping error caused by imperfections in a quartz crystal oscillator. In the case of the OBS, the clock module's quartz oscillator is designed to vibrate at a nominal frequency of 32,768 Hz, but the actual frequency in any given device almost never matches this value exactly. Therefore, we first calculate the deviation from the nominal frequency to compensate for the oscillator's frequency offset. Using Eq. (S1), we integrate the deviation between the nominal and measured frequencies over the recording period to estimate the cumulative timing error and correct the time stamps of all seismic traces accordingly.

A second component of drift arises from quartz aging, which is nonlinear and influenced by factors such as temperature and pressure. To correct for this effect, we estimate the clock drift (lag time) using ambient-noise cross-correlation between the OBS units and the nearby land station TOLI2 to obtain the drift curve (Hable et al., 2018). Specifically, we implemented the procedure proposed by Bensen et al. (2007) to compute cross-correlation functions from ambient-noise data.

To validate our time-correction results, we compare the cross-correlation functions before and after applying the correction for OBS stations M01G and M02F (Fig. S1). The comparison shows that both the oscillator frequency offset and the time drift caused by quartz aging are effectively corrected.

Main frequency deviation: The accumulated error due to the deviation of the internal oscillator frequency from the standard frequency was corrected by comparing the measured frequency ($PClk$) with the reference frequency ($PClk_0$).

Phase filter delay: During sampling, the phase filter introduces a delay equivalent to 18 sampling points for all OBSs, with each point corresponding to the sampling interval Δt.

Combining these terms, the total time error is expressed as:

$$Time_{Err} = Clock_{Err} + \frac{(PClk - PClk_0)\cdot(npts\cdot\Delta t)}{PClk_0} - 18\Delta t, \qquad \text{(Eq. S1)}$$

where $npts$ is the total number of sampling points. In our deployment, the sampling rate of the OBSs was 50 Hz, corresponding to a sampling interval of $\Delta t = 0.02s$. This information has been added to the revised manuscript to clarify the time correction procedure.

Text S2: Azimuth correction

In the ideal case, the energy of the direct P wave approaches zero on the transverse component (Wang et al., 2016). Therefore, when one of the OBS horizontal components is rotated to the transverse direction, the P-wave energy reaches its minimum, and the two horizontal components can then be identified as the radial and transverse components of the seismic wavefield. Using the station and event location information, the back-azimuth can be obtained, allowing the radial and transverse components to be further rotated into the true north and east directions.

Figure S2a illustrates the coordinate system from the source to the OBS and the propagation (particle motion) direction of the P wave. A rotation step of 0.1° was applied to rotate the N–E coordinate system into the R–T coordinate system. We employed an SNR-weighted multi-event method to perform a grid search for the optimal back-azimuth angle θ_a. At each grid point, the P-wave transverse component energy was calculated as $E_\mathrm{T}(\theta_\mathrm{a})$.

$$E(\theta_{\mathrm{a}}) = \frac{\sum_{i=1}^{N} w_i E_{\mathrm{T}}^{i}(\theta_{\mathrm{a}})}{\sum_{i=1}^{N} w_i}, \quad \text{(Eq. S2)}$$

Text S3: Voronoi cell

In our inversions the model is a d-dimensional vector $\mathrm{m} = [m_1, \ldots, m_d]^{\top}$ whose components are the parameters being inverted (e.g., layer thicknesses h_i, and shear-wave velocities $V_{s,i}$) Given a set of sampled models $\{\mathrm{m}_j\}_{j=1}^{n_p}$, the Voronoi cell associated with m_j is the convex polyhedron (Sambridge, 1999a; Sambridge, 1999b):

$$V(\mathrm{m}_j) = \{\mathrm{x} \mid \|\mathrm{x} - \mathrm{m}_j\| \le \|\mathrm{x} - \mathrm{m}_i\|, i \ne j\}, \quad \text{(Eq. S3)}$$

where the distance is defined by $\|\mathrm{m}_a - \mathrm{m}_b\| = [(\mathrm{m}_a - \mathrm{m}_b)^{\top} \mathrm{C}_M^{-1} (\mathrm{m}_a - \mathrm{m}_b)]^{1/2}$. The matrix C_M non-dimensionalizes and scales each parameter (typically a diagonal matrix with elements $1/s_i^2$). The set of Voronoi cells uniquely and fully partitions the model space; cell sizes are inversely related to the local sampling density. Following the neighbourhood approximation, we approximate the misfit by assigning a constant value within each cell equal to the misfit at its generating sample m_j. New samples therefore only modify the cells locally and progressively increase the resolution in regions of lower misfit.

References

Bonvalot, S., Briais, A., Peyrefitte, A., Biancale, R., Gabalda, G., Moreaux, G., Sarrailh, M., and Fayard, T.: World Gravity Map (WGM) Project: Objectives and Status, American Geophysical Union., G23C-0698, 2009

Wang, X., Chen, Q.F., Li, J., and Wei, S.J.: Seismic sensor misorientation measurement using P-wave particle motion: An application to the NECsaids Array, Seismological Research Letters., 87, 901–911, doi:10.1785/0220160005, 2016.

Sambridge, M.: Geophysical inversion with a neighbourhood algorithm–I. Searching a parameter space, Geophysical Journal International., 138, 479–494, doi:10.1046/j.1365-246X.1999.00876.x, 1999a.

Sambridge, M.: Geophysical inversion with a neighbourhood algorithm–II. Appraising the ensemble, Geophysical Journal International., 138, 727–746, doi:10.1046/j.1365-246X.1999.00900.x, 1999b.